energies

MDPI

Article

Power Quality Analysis of a Hybrid Microgrid-Based SVM Inverter-Fed Induction Motor Drive with Modulation Index Diversification

Subramanian Vasantharaj [1], Vairavasundaram Indragandhi [1,*], Mohan Bharathidasan [1] and Belqasem Aljafari [2]

[1] School of Electrical Engineering, Vellore Institute of Technology, Vellore 632 014, India
[2] Department of Electrical Engineering, Najran University, Najran 11001, Saudi Arabia
* Correspondence: indragandhi.v@vit.ac.in

Abstract: The effects of varying modulation indices on the current and voltage harmonics of an induction motor (IM) powered by a three-phase space vector pulse-width modulation (SVM) inverter are presented in this research. The effects were examined using simulation and an experimental setup. IMs can be governed by an SVM inverter drive or a phase-angle control drive for applications that require varying speeds. The analysis of THD content in this study used the modulation index (MI), whose modification affects the harmonic content, and voltage-oriented control (VOC) with SVM in three-phase pulse-width modulation (PWM) inverters with fixed switching frequencies. The control technique relies on two cascaded feedback loops, one controlling the grid current and the other regulating the dc-link voltage to maintain the required level of dc-bus voltage. The control strategy was developed to transform between stationary (α–β) and synchronously rotating (d–q) coordinate systems. To test the viability of the suggested control technique, a 1-hp/3-phase/415-V experimental prototype system built on the DSPACE DS1104 platform was created, and the outcomes were evaluated with sinusoidal pulse-width modulation (SPWM).

Keywords: induction motor drive; dc-link voltage balancing; space vector modulation; switching loss; total harmonic distortion

check for updates

Citation: Vasantharaj, S.; Indragandhi, V.; Bharathidasan, M.; Aljafari, B. Power Quality Analysis of a Hybrid Microgrid-Based SVM Inverter-Fed Induction Motor Drive with Modulation Index Diversification. *Energies* **2022**, *15*, 7916. https://doi.org/10.3390/en15217916

Academic Editor: Adolfo Dannier

Received: 25 September 2022
Accepted: 21 October 2022
Published: 25 October 2022

1. Introduction

Electric motors are used in many driving components worldwide, accounting for 40% to 50% of all electricity demand [1]. Seventy percent of the electricity needed to run industrial loads is provided by three-phase IMs [2]. Due to their appealing qualities, such as low cost, straightforward design, excellent reliability, and ease of maintenance, electric motor sales have climbed to 85% [3–5]. Although direct current (DC) motors are frequently seen in applications involving variable speed operations because of how simple it is to control torque and field flux with armature and field current, these motors possess the drawback of having a commutator and brushes that could cause corrosion and necessitate regular maintenance [6]. Due to their high output power, toughness, robustness, efficiency, affordability, capacity to tolerate hazardous or severe working situations, and ruggedness, IMs do not experience DC motor difficulties [7]. The abrupt variation in load, which uses a significant amount of electricity and raises the cost of energy, impacts the functioning of three-phase IMs [8]. To regulate speed and preserve high efficiency, a variable speed drive (VSD) may be employed [9]. Moreover, the controller and switching technique employed in VSD significantly impact the achievability of high efficiency and reliability for IMs [10,11]. Pulse-width modulation (PWM) techniques are often used to control the switches of voltage source inverters (VSIs), as well as the frequency and output voltage of IMs [12]. One of the better approaches for VSI is the SVM switching approach, which has reduced switching losses and the capacity to reduce the harmonic output signals generated by inverters [13].

Recent studies have proposed several control techniques for PWM rectifiers to enhance the input power factor and transform the input current into a sinusoidal waveform. Numerous PWM modulation techniques are in use, including sinusoidal PWM and the space vector method. Technically, the SVM methodology is the optimal modulation method overall. Compared to the conventional PWM approach, the harmonic distortion of current decreases with the SVM. The duty cycles of VSI switches have been determined via the SVM, using the space vector concept. The only things to have been digitally implemented are PWM modulators. The possibility of straightforward digital implementation and a large linear modulation range for line-to-line voltages are the distinguishing features of SVM. Despite the SVPWM technique's benefits over PWM, new techniques are continually being developed. The main objective [14] has been to find efficient methods to provide output voltages with low harmonic rates and less switch-level loss.

The voltage-oriented control (VOC) algorithm, which is well known among indirect power control algorithms that use current controllers and is equivalent to the field-oriented control (FOC) of the IM, is able to generate high dynamic and static performance by using internal current control loops and an outer voltage control loop. The basis of VOC is the orientation of the rotating synchronous reference frame with respect to the grid line voltage vector. The suggested VOC approach exhibits highly dynamic behavior, suitable output voltage, and a low input current THD [15,16].

The proper operation of the control system has generally been hampered by the hardware execution of the IM drive controller. Digital signal processors (DSPs) and field programmable gate arrays (FPGAs) are two integrated circuits that have been used extensively in control platforms [17,18]. Implementing a user-friendly control unit for online supervision and monitoring is now possible due to the presence of a graphical object-oriented package (Control Desk software) on a dSPACE system. The automation and automotive sectors both use the dSPACE system, which is extremely popular among controlling platforms. The development of PV standalone inverters uses the dSPACE system as a control platform as an additional application area. In this study, the SVM control method is demonstrated through a simulation to support actual inverter hardware. The Simpowersystems and dSPACE DS1104 blockset libraries were used in the simulation, performed in the Simulink/MATLAB environment.

The remaining sections of this article are organized as follows: A description of an IM drive is given in Section 2. Section 3 explains the VOC control for a three-phase VSI. A VSI using the SVM approach is introduced in Section 4. Section 5 contains the simulation and experimental discussion. Section 6 summarizes the research and presents the findings.

2. Overview of the Induction Motor Drive

The squirrel-cage three-phase IM is an asynchronous AC motor that operates on electromagnetic induction principles. The IM's primary purpose is to convert electrical energy into mechanical energy. A small air gap separates the stator and the rotor, the two components that make up the IM. The three-phase squirrel-cage IM [19–21] is the one most often used due to its insulated winding in both stator and rotor, which are formed of cast and solid bars with high conductivity, as shown in Figure 1.

For the rotor to rotate at synchronous speed (ω_{sm} in rad/s), where $\omega_{sm} = 2\pi f$ (rad/s), where f = synchronous frequency, three-phase voltages must first be applied to the stator winding. The stator currents produce a revolving magnetic field in the magnetic circuit, formed by the air gap between the stator and rotor cores. The number of poles (P) affects the mechanical synchronous speed (ω_{sm} in rad/s). This is how the synchronous speed is determined [22].

$$\omega_{sm} = \frac{2\omega_s}{P} \tag{1}$$

$$N_{sm} = \frac{120f}{P} \tag{2}$$

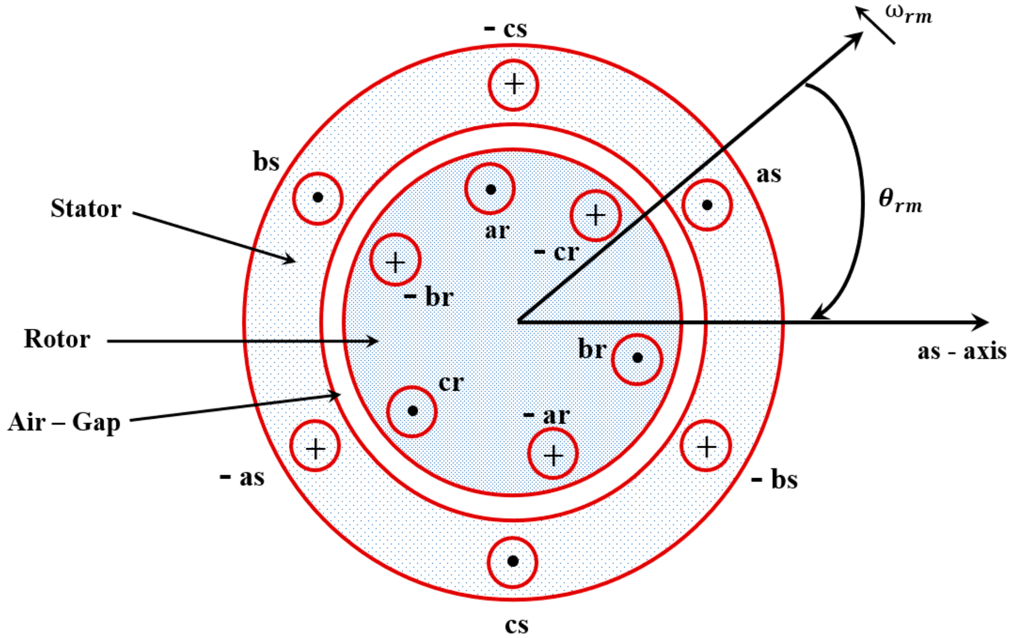

Figure 1. Three-phase IM cross-sectional model.

Modelling of the Induction Motor

To depict the physical systems, the computer models the mathematical model of the three-phase IM and its driving system [4]. The control parameters of the models are highlighted in this three-phase IM modelling. For the three-phase IM, the magnetic connection between the stator and rotor voltage equations can be expressed as follows [23].

$$V_{as} = i_{as} r_s + \frac{d\lambda_{as}}{dt};\ V_{bs} = i_{bs} r_s + \frac{d\lambda_{bs}}{dt};\ V_{cs} = i_{cs} r_s + \frac{d\lambda_{cs}}{dt} \quad (3)$$

$$V_{ar} = i_{ar} r_r + \frac{d\lambda_{ar}}{dt};\ V_{br} = i_{br} r_r + \frac{d\lambda_{br}}{dt};\ V_{cr} = i_{cr} r_r + \frac{d\lambda_{cr}}{dt} \quad (4)$$

where V_{as}, V_{bs}, V_{cs} = 3-φ stator voltages; V_{ar}, V_{br}, V_{cr} = 3-φ rotor voltages; i_{as}, i_{bs}, i_{cs} = 3-φ stator currents; i_{ar}, i_{br}, i_{cr} = 3-φ rotor currents; r_s = stator resistance; r_r = rotor resistance; λ_{as}, λ_{bs}, λ_{cs} = flux linkages of the stator; and λ_{ar}, λ_{br}, λ_{cr} = flux linkages of the rotor.

According to the winding currents and inductances, the flux linkages indicate the matrix formed between the rotor and stator windings, as depicted in the following matrix [24].

$$\begin{bmatrix} \lambda_s^{abc} \\ \lambda_r^{abc} \end{bmatrix} = \begin{bmatrix} L_{ss}^{abc} & L_{sr}^{abc} \\ L_{rs}^{abc} & L_{rr}^{abc} \end{bmatrix} \begin{bmatrix} i_s^{abc} \\ i_r^{abc} \end{bmatrix} \quad (5)$$

where $\lambda_s^{abc} = \begin{bmatrix} \lambda_{as} & \lambda_{bs} & \lambda_{cs} \end{bmatrix}^{\mathrm{T}}, i_s^{abc} = \begin{bmatrix} i_{as} & i_{bs} & i_{cs} \end{bmatrix}^{\mathrm{T}}, \lambda_r^{abc} = \begin{bmatrix} \lambda_{ar} & \lambda_{br} & \lambda_{cr} \end{bmatrix}^{\mathrm{T}}, i_r^{abc} = \begin{bmatrix} i_{ar} & i_{br} & i_{cr} \end{bmatrix}^{T}$, and superscript T = transpose of the array; L_{ss}^{abc} = stator-to-stator winding inductance; L_{rr}^{abc} = rotor-to-rotor winding inductance; and L_{sr}^{abc} = stator-to-rotor mutual inductance, which depends on the rotor angle θ_r.

To solve and simplify the computation of the three-phase IM performance, contemporary research analyzes the transient and steady-state performance of three Ims with a direct-quadrature-zero ($dq0$) stationary motor model [21,25,26]. As it can accurately represent the real-time motor model, a $dq0$ reference frame is chosen in this study to create the motor simulation model. The relationship between the rotor $dq0$ and the abc stator axes is shown in Figure 2. The mechanical rotor speed is denoted by ω_{rm}, and the reference frame speed is represented by ω. The transformation from abc to $dq0$ is analyzed using stationary and synchronously revolving frames. Similar to those typically used for supply networks, the stationary rotating frame has a speed frame that produces a value of ω = 0. When the synchronous reference frame revolves in the same direction as the rotor revolution, the speed frame becomes $\omega = \omega_s$. The matrix below contains their inverses and the transition from the *abc* to the *dq*0 reference frame [27].

$$\begin{bmatrix} x_d \\ x_q \\ x_0 \end{bmatrix} = \frac{2}{3}\begin{bmatrix} cos\ (\theta) & cos\ \left(\theta - \frac{2\pi}{3}\right) & cos\ \left(\theta + \frac{2\pi}{3}\right) \\ sin\ (\theta) & sin\ \left(\theta - \frac{2\pi}{3}\right) & sin\ \left(\theta + \frac{2\pi}{3}\right) \\ \frac{1}{2} & \frac{1}{2} & \frac{1}{2} \end{bmatrix}\begin{bmatrix} x_a \\ x_b \\ x_c \end{bmatrix} = \left[X_{dq0}(\theta)\right]\begin{bmatrix} x_a \\ x_b \\ x_c \end{bmatrix} \quad (6)$$

$$\begin{bmatrix} x_a \\ x_b \\ x_c \end{bmatrix} = \frac{2}{3}\begin{bmatrix} cos\ (\theta) & sin\ (\theta) & 1 \\ cos\ \left(\theta - \frac{2\pi}{3}\right) & sin\ \left(\theta - \frac{2\pi}{3}\right) & 1 \\ cos\ \left(\theta + \frac{2\pi}{3}\right) & sin\ \left(\theta + \frac{2\pi}{3}\right) & 1 \end{bmatrix}\begin{bmatrix} x_d \\ x_q \\ x_0 \end{bmatrix} = \left[X_{dq0}(\theta)\right]^{-1}\begin{bmatrix} x_a \\ x_b \\ x_c \end{bmatrix} \quad (7)$$

where variable x = the 3-φ IM's phase voltage, current, or flux linkage. The stator voltages are converted to the *dq*0 voltages into a matrix form that includes flux linkages, currents, and voltages of the *dq*0 reference frame to produce the *dq*0 voltages [28].

$$\begin{bmatrix} v_{ds} \\ v_{qs} \\ v_{0s} \end{bmatrix} = \frac{d\theta}{dt}\begin{bmatrix} 0 & 1 & 0 \\ -1 & 0 & 0 \\ 0 & 0 & 0 \end{bmatrix}\begin{bmatrix} \lambda_{ds} \\ \lambda_{qs} \\ \lambda_{0s} \end{bmatrix} + \frac{d}{dt}\begin{bmatrix} \lambda_{ds} \\ \lambda_{qs} \\ \lambda_{0s} \end{bmatrix} + r_s\begin{bmatrix} 1 & 0 & 0 \\ 0 & 1 & 0 \\ 0 & 0 & 1 \end{bmatrix}\begin{bmatrix} i_{ds} \\ i_{qs} \\ i_{0s} \end{bmatrix} \quad (8)$$

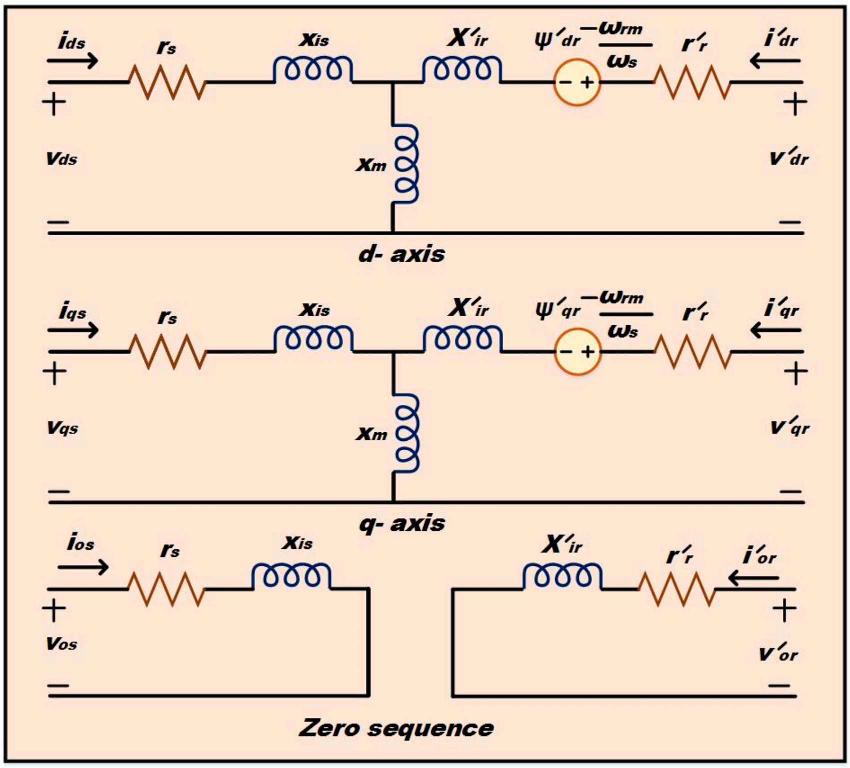

Figure 2. Equivalent circuits of the three-phase IM's *dq*0 stationary reference frames.

Similar to this, while transferring the voltages, currents, and flux linkages, the rotor voltages are converted to the *dq*0 frame into a matrix form that must be combined with the mechanical rotor angle $(\theta - \theta_{rm})$ to become $[X_{dq0}(\theta - \theta_{rm})]$ in order to achieve the subsequent equations shown below [29].

$$\begin{bmatrix} v_{dr} \\ v_{qr} \\ v_{0r} \end{bmatrix} = \frac{d(\theta - \theta_{rm})}{dt}\begin{bmatrix} 0 & 1 & 0 \\ -1 & 0 & 0 \\ 0 & 0 & 0 \end{bmatrix}\begin{bmatrix} \lambda_{dr} \\ \lambda_{qr} \\ \lambda_{0r} \end{bmatrix} + \frac{d}{dt}\begin{bmatrix} \lambda_{dr} \\ \lambda_{qr} \\ \lambda_{0r} \end{bmatrix} + r_s\begin{bmatrix} 1 & 0 & 0 \\ 0 & 1 & 0 \\ 0 & 0 & 1 \end{bmatrix}\begin{bmatrix} i_{dr} \\ i_{qr} \\ i_{0r} \end{bmatrix} \quad (9)$$

The stator *abc* flux linkage is transformed to produce the stator *dq*0 flux linkages, which are stated as follows.

$$\begin{bmatrix} \lambda_{ds} \\ \lambda_{qs} \\ \lambda_{0s} \end{bmatrix} = \begin{bmatrix} L_{ls} + \frac{3}{2}L_{ss} & 0 & 0 \\ 0 & L_{ls} + \frac{3}{2}L_{ss} & 0 \\ 0 & 0 & L_{ls} \end{bmatrix} \begin{bmatrix} i_{ds} \\ i_{qs} \\ i_{0s} \end{bmatrix} + \begin{bmatrix} \frac{3}{2}L_{sr} & 0 & 0 \\ 0 & \frac{3}{2}L_{sr} & 0 \\ 0 & 0 & 0 \end{bmatrix} \begin{bmatrix} i_{dr} \\ i_{qr} \\ i_{0r} \end{bmatrix} \tag{10}$$

The rotor *dq*0 flux linkages are produced in a similar manner to the rotor *abc* flux linkage.

$$\begin{bmatrix} \lambda_{dr} \\ \lambda_{qr} \\ \lambda_{0r} \end{bmatrix} = \begin{bmatrix} \frac{3}{2}L_{sr} & 0 & 0 \\ 0 & \frac{3}{2}L_{sr} & 0 \\ 0 & 0 & 0 \end{bmatrix} \begin{bmatrix} i_{ds} \\ i_{qs} \\ i_{0s} \end{bmatrix} + \begin{bmatrix} L_{lr} + \frac{3}{2}L_{rr} & 0 & 0 \\ 0 & L_{lr} + \frac{3}{2}L_{rr} & 0 \\ 0 & 0 & L_{lr} \end{bmatrix} \begin{bmatrix} i_{dr} \\ i_{qr} \\ i_{0r} \end{bmatrix} \tag{11}$$

The stator and rotor *dq*0 flux linkage relations can be stated as in Equation (12) [25], where $\lambda'_{dr}, \lambda'_{qr}$ are the reference values on the stator side of the *dq* rotor flux linkages. This is based on Equations (10) and (11); the referred values on the stator side of the *dq* rotor currents are i'_{dr}, i'_{qr}.

$$\begin{bmatrix} \lambda_{ds} \\ \lambda_{qs} \\ \lambda_{0s} \\ \lambda'_{dr} \\ \lambda'_{qr} \\ \lambda'_{0r} \end{bmatrix} = \begin{bmatrix} L_{ls} + L_m & 0 & 0 & L_m & 0 & 0 \\ 0 & L_{ls} + L_m & 0 & 0 & L_m & 0 \\ 0 & 0 & L_{ls} & 0 & 0 & 0 \\ L_m & 0 & 0 & L'_{lr} + L_m & 0 & 0 \\ 0 & L_m & 0 & 0 & L'_{lr} + L_m & 0 \\ 0 & 0 & 0 & 0 & 0 & L'_{lr} \end{bmatrix} \begin{bmatrix} i_{ds} \\ i_{qs} \\ i_{0s} \\ i'_{dr} \\ i'_{qr} \\ i'_{0r} \end{bmatrix} \tag{12}$$

The governing equations [27] are produced by converting the final *dq*0 reference frame equations to the flux linkage, utilizing the formula $\psi = \omega_s \lambda$, and the inductance into reactance, using $x = \omega_s L$.

$$v_{ds} = \frac{1}{\omega_s}\frac{d\psi_{ds}}{dt} + \frac{\omega}{\omega_s}\psi_{qs} + r_s i_{ds} \tag{13}$$

$$v_{qs} = \frac{1}{\omega_s}\frac{d\psi_{qs}}{dt} + \frac{\omega}{\omega_s}\psi_{ds} + r_s i_{qs} \tag{14}$$

$$v_{0s} = \frac{1}{\omega_s}\frac{d\psi_{0s}}{dt} + r_s i_{0s} \tag{15}$$

$$v'_{dr} = \frac{1}{\omega_s}\frac{d\psi'_{dr}}{dt} + \left(\frac{\omega - \omega_{rm}}{\omega_s}\right)\psi'_{qr} + r'_r i'_{dr} \tag{16}$$

$$v'_{qr} = \frac{1}{\omega_s}\frac{d\psi'_{qr}}{dt} - \left(\frac{\omega - \omega_{rm}}{\omega_s}\right)\psi'_{dr} + r'_r i'_{qr} \tag{17}$$

$$v'_{0r} = \frac{1}{\omega_s}\frac{d\psi'_{0r}}{dt} + r'_r i'_{0r} \tag{18}$$

$$\begin{bmatrix} \psi_{ds} \\ \psi_{qs} \\ \psi_{0s} \\ \psi'_{dr} \\ \psi'_{qr} \\ \psi'_{0r} \end{bmatrix} = \begin{bmatrix} x_{ls} + x_m & 0 & 0 & x_m & 0 & 0 \\ 0 & x_{ls} + L_m & 0 & 0 & x_m & 0 \\ 0 & 0 & x_{ls} & 0 & 0 & 0 \\ x_m & 0 & 0 & x'_{lr} + x_m & 0 & 0 \\ 0 & x_m & 0 & 0 & x'_{lr} + x_m & 0 \\ 0 & 0 & 0 & 0 & 0 & x'_{lr} \end{bmatrix} \begin{bmatrix} i_{ds} \\ i_{qs} \\ i_{0s} \\ i'_{dr} \\ i'_{qr} \\ i'_{0r} \end{bmatrix}. \tag{19}$$

The electromagnetic torque can manifest itself in the following ways:

$$\begin{aligned} T_{em} &= \frac{3}{2}\frac{P}{2\omega_s}\left(\psi'_{dr} i'_{qr} - \psi'_{qr} i'_{dr}\right) \\ &= \frac{3}{2}\frac{P}{2\omega_s}\left(\psi_{qs} i_{ds} - \psi_{ds} i_{qs}\right) \\ &= \frac{3}{2}\frac{P}{2\omega_s} x_m \left(i'_{qr} i_{ds} - i'_{dr} i_{qs}\right) \end{aligned} \tag{20}$$

As depicted in Figure 2, the equivalent circuits of the $dq0$ stationary reference frames are generated by introducing Equation (19) into Equation (13) to Equation (18).

3. Voltage-Oriented Control

The VOC technique for AC-DC converters is derived from FOC for IMs. FOC provides a quick, dynamic reaction due to the utilization of current control loops. The theoretical elements of the VOC approach used for grid-connected rectifiers have received extensive coverage. The control system uses the PWM technique to ensure that the characteristics of the VOC control scheme are modified. It is possible to reduce the impact of interference (disturbances). By using the hysteresis pulse-width modulation approach, system solidity can be achieved. Power switching is stressed as a result of the fluctuating switching frequency, necessitating the use of an input filter at high-value parameters. To alleviate harmonic issues, the proposed method utilizes the VOC principle to regulate charging while maintaining low harmonic distortions to the grid. Figure 3 depicts VOC for AC-DC line-side converters. VOC operates most frequently in the two-phase zero and $dq0$ domains, where the Clarke and Park transformation matrices are employed.

$$\begin{bmatrix} V_{s\alpha} \\ V_{s\beta} \\ V_0 \end{bmatrix} = \sqrt{\frac{2}{3}} \begin{bmatrix} 1 & -\frac{1}{2} & -\frac{1}{2} \\ 0 & \frac{\sqrt{3}}{2} & -\frac{\sqrt{3}}{2} \\ \frac{1}{\sqrt{2}} & \frac{1}{\sqrt{2}} & \frac{1}{\sqrt{2}} \end{bmatrix} \begin{bmatrix} V_{sa} \\ V_{sb} \\ V_{sc} \end{bmatrix} \tag{21}$$

$$\begin{bmatrix} V_d \\ V_q \end{bmatrix} = \begin{bmatrix} sin(\theta) & cos(\theta) \\ -cos(\theta) & sin(\theta) \end{bmatrix} \begin{bmatrix} V_{s\alpha} \\ V_{s\beta} \end{bmatrix} \tag{22}$$

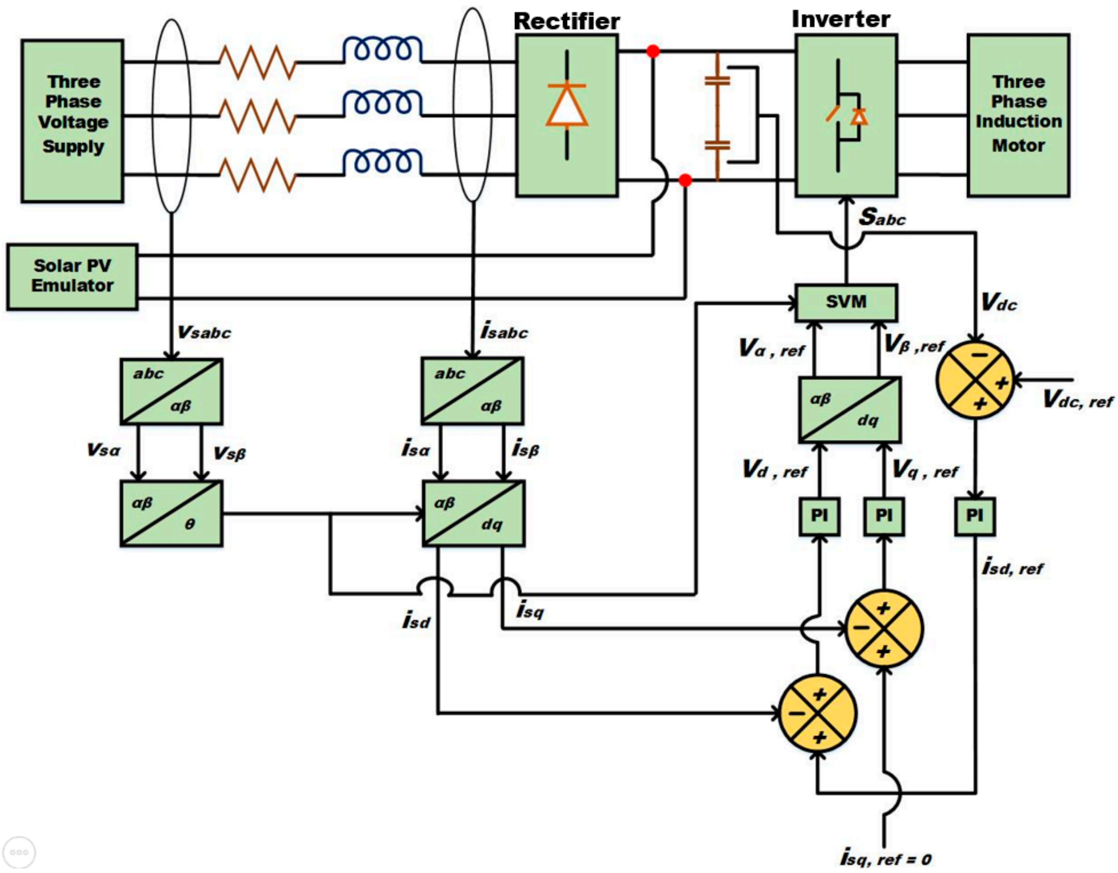

Figure 3. Overall control structure of VOC of a PWM inverter [30].

Note that V_{sa}, V_{sb}, and V_{sc} = 3-φ source voltages in the *abc* domain, while $V_{s\alpha}$, $V_{s\beta}$, and V_0 = source voltages in the $\alpha\beta0$ domain. V_d, V_q, and V_0 are source voltages of the $dq0$ domain, and θ = the operating phase of the power system. As shown in Figure 2, an equivalent transformation procedure is used to transform the 3-φ source current i_{sabc}.

Based on the following techniques, steady-state errors are easily reduced by the proportional integral (PI) controllers by employing the transformation technique to convert AC-side control variables into DC signals:

$$v_{d,ref} = K_p\left(i_{sd,ref} - i_{sd}\right) + K_i \int \left(i_{sd,ref} - i_{sd}\right)dt \tag{23}$$

$$v_{q,ref} = K_p\left(i_{sq,ref} - i_{sq}\right) + K_i \int \left(i_{sq,ref} - i_{sq}\right)dt \tag{24}$$

where K_p and K_i = gains of the PI controller, i_{sd} and i_{sq} = source current in the $dq0$ domain, and $i_{sd,ref}$ and $i_{sq,ref}$ = reference signals for i_{sd} and i_{sq}, respectively. After obtaining the reference voltages $v_{d,ref}$ and $v_{q,ref}$, the gate switching pulses S_{abc}, which regulate the operation of the VOC inverter, are derived using the PWM switching approach and the inverse park transformation as given in Equation (25).

$$\begin{bmatrix} V_{\alpha,ref} \\ V_{\beta,ref} \end{bmatrix} = \begin{bmatrix} sin(\theta) & -cos(\theta) \\ cos(\theta) & sin(\theta) \end{bmatrix} \begin{bmatrix} v_{d,ref} \\ v_{q,ref} \end{bmatrix} \tag{25}$$

4. SVM Switching Techniques

The SVM approach, generally acknowledged as the optimum method for variable speed drive applications, creates PWM control signals in the 3-φ inverter. Compared to other PWM systems, this method provides an enhanced means of achieving a high output voltage, minimizing the harmonic output, and lowering switching losses. As a result, the SVM technique is confirmed as the best approach for reducing harmonic distortion [31–33].

$$\begin{bmatrix} V_{ab} \\ V_{bc} \\ V_{ca} \end{bmatrix} = V_{dc} \begin{bmatrix} 1 & -1 & 0 \\ 0 & 1 & -1 \\ -1 & 0 & 1 \end{bmatrix} \begin{bmatrix} s_1 \\ s_3 \\ s_5 \end{bmatrix} \tag{26}$$

$$\begin{bmatrix} V_{ab} \\ V_{bc} \\ V_{ca} \end{bmatrix} = \frac{V_{dc}}{3} \begin{bmatrix} 2 & -1 & -1 \\ -1 & 2 & -1 \\ -1 & -1 & 2 \end{bmatrix} \begin{bmatrix} s_1 \\ s_3 \\ s_5 \end{bmatrix} \tag{27}$$

Eight switch variables can be created using the inverter's six IGBTs. Six switch variables—$V_1, V_2, \ldots, V_6$, and the last two—are zero vectors chosen for the three upper IGBT switches. The on and off patterns of the lower IGBT switches are the opposite of those of the higher switches. Figure 4 displays the eight switching vectors of the SVM [34].

The output waveform of the inverter is split into six hexagonal sectors, according to the SVM's working principle. The sector angle is 60° apart, and every sector is between two voltage space vectors (Figure 5) [35]. The SVM approach receives a 3-φ voltage (V_a, V_b, and V_c) with a 120° angle among the 2-φ and transforms it into 2-φ (V_α and V_β) with a 90° using Clark's transformation (Figure 6a).

To make the study of three-phase voltage more straightforward, 2-φ voltages (V_α and V_β) are used as part of a scientific transformation. The voltages are used to calculate the hexagon's voltage vector angle (α) and the reference voltage vector's magnitude (V_{ref}). V_{ref} is assumed as the magnitude of the V_α and V_β voltages, while α is the frequency of V_α and V_β. V_{ref} and α are situated among the two neighboring non-zero and zero vectors. The following formulas can be used to calculate them [29].

$$\begin{bmatrix} V_\alpha \\ V_\beta \end{bmatrix} = \frac{2}{3} \begin{bmatrix} 1 & \frac{-1}{2} & \frac{-1}{2} \\ 0 & \frac{\sqrt{3}}{2} & -\frac{\sqrt{3}}{2} \end{bmatrix} \begin{bmatrix} V_a \\ V_b \\ V_c \end{bmatrix} \tag{28}$$

$$\left|V_{ref}\right| = \sqrt{V_\alpha^2 + V_\beta^2} \tag{29}$$

$$\alpha = tan^{-1}\frac{V_\beta}{V_\alpha} \tag{30}$$

Sector 1 contains the vectors that can be used to synthesize V_{ref}, which is located here.

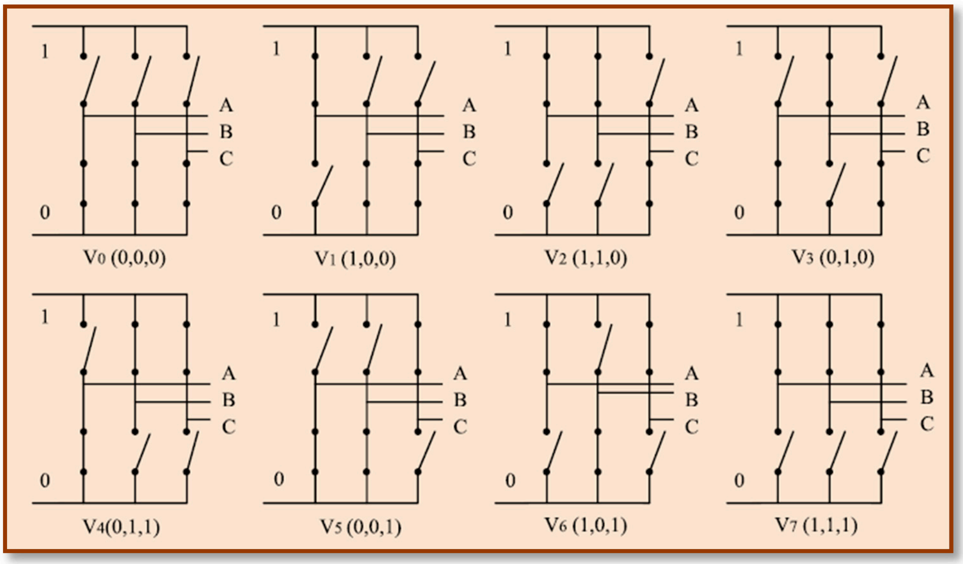

Figure 4. Eight switching states for the inverter voltage vectors (V_0 to V_7).

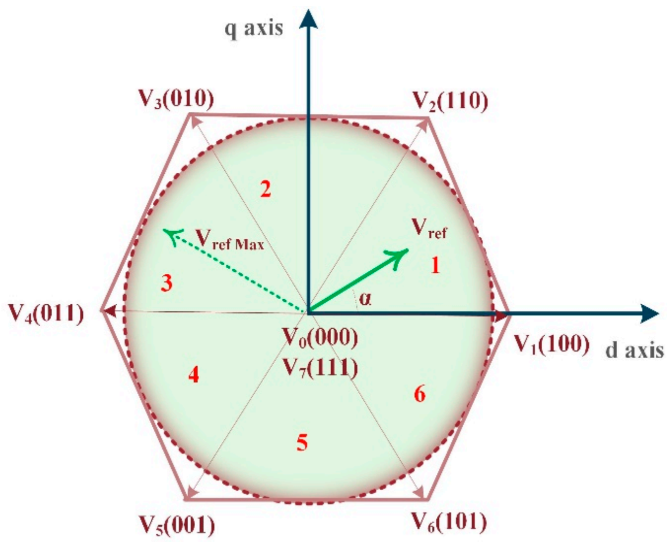

Figure 5. Space vector diagram.

The relevant space vectors and time intervals (T_1, T_2, and T_0) in sector 1 are depicted in Figure 6b. The duration of Vref is calculated by multiplying the reference voltage by the sampling time period, which is equivalent to the sum of the voltages times the time interval of the space vectors in the specified sector [36].

$$\int_0^{T_s} \overline{V}_{ref} dt = \int_0^{T_1} \overline{V}_1 dt + \int_{T_1}^{T_1+T_2} \overline{V}_2 dt + \int_{T_1+T_2}^{T_s} \overline{V}_0 dt T_s = T_1 + T_2 + T_0 \tag{31}$$

where *Ts* = switching time, which is calculated by *Ts* $=\frac{1}{f_s}$, and *fs* = switching frequency.

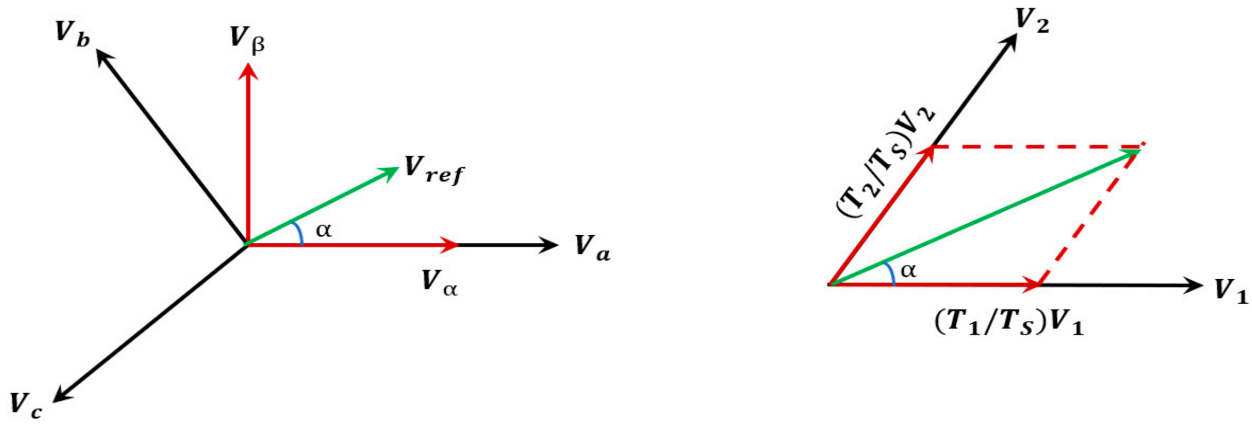

(a) (b)

Figure 6. (**a**) Space vector diagram. (**b**) Space of sector-1 between V_1 and V_2.

Equation (30) illustrates how $\overline{V_0}$ provides zero voltage to the output load. As a result, the equation is:

$$T_s\overline{V}_{ref} = T_1\overline{V}_1 + T_2\overline{V}_2 \tag{32}$$

When the values of $\overline{V_1}$ and $\overline{V_2}$ are substituted into the $\alpha\beta$ frame and the voltage vectors are evaluated, the results are as follows [37].

$$T_s\left|V_{ref}\right|\begin{bmatrix}cos(\alpha)\\ sin(\alpha)\end{bmatrix} = T_1\frac{2}{3}V_{dc}\begin{bmatrix}1\\ 0\end{bmatrix} + T_2\frac{2}{3}V_{dc}\begin{bmatrix}cos\frac{\pi}{3}\\ sin\frac{\pi}{3}\end{bmatrix} \tag{33}$$

$$T_1 = T_s\frac{3}{2}\frac{\left|V_{ref}\right|}{V_{dc}}\frac{sin\left(\frac{\pi}{3}-\alpha\right)}{sin\left(\frac{\pi}{3}\right)} \tag{34}$$

$$T_2 = T_s\frac{3}{2}\frac{\left|V_{ref}\right|}{V_{dc}}\frac{sin(\alpha)}{sin\left(\frac{\pi}{3}\right)} \tag{35}$$

The relation between the magnitude of the reference voltage and the *dc* voltage value represented by the following equation is known as the MI for the SVM [38].

$$MI = \frac{\left|V_{ref}\right|}{\frac{2}{\pi}V_{dc}} \tag{36}$$

Equation (35) can be substituted into Equations (33) and (34) to determine the time duration in the other sectors (n), and 60 degrees with α can be used for each sector to obtain the result [39,40].

$$T_1 = \frac{\sqrt{3}T_s\left|V_{ref}\right|}{V_{dc}}sin\left(\frac{n}{3}\pi-\alpha\right) \tag{37}$$

$$T_2 = \frac{\sqrt{3}T_s\left|V_{ref}\right|}{V_{dc}}sin\left(\alpha-\frac{n-1}{3}\pi\right) \tag{38}$$

$$T_0 = T_s - (T_1+T_2) \tag{39}$$

Alternating the zero-vector sequence, the asymmetric sequence, the maximum current not switched sequence, and the right aligned sequence are the four different types of switching patterns. To reduce device switching frequency, all switching patterns must fulfill the following two requirements. Merely two switches in the same inverter leg are used to switch from one switching state to another. To minimize the switching frequency, one of the switches must be turned off if the other is activated. The least amount of switching is necessary to move V_{ref} from one sector to the next to minimize switching losses. The optimum strategy, according to research, is the symmetric sequence method, since it minimizes switching losses. The generation of the SVM signal and the inverter output voltages and a comparison of the duty ratio waveform's three signals with the triangle waveform is shown in Figure 7. This comparison assumes that S is ON if $V_{DutyRatio} > V_{triangle}$; otherwise, S is OFF.

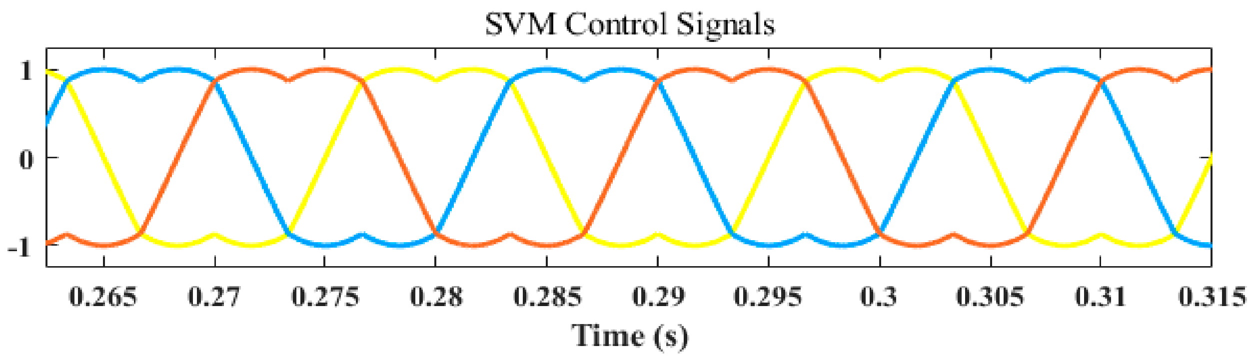

Figure 7. SVM waves for a three-phase inverter.

Every switch in a bipolar switching scheme operates in opposition to the facing switch, as seen in the example where the triangle waveform and the $V_{TaDutyRatio}$ are compared to produce the PWM signal for the IGBT1 and the opposing IGBT4 in leg 1, which is identical to leg 2 and leg 3.

5. Results and Discussion

5.1. Simulation Results

In the simulation studies, several experiments were carried out to confirm the effectiveness of the suggested VOC system. The DG capacities of the MG test system taken into consideration in this work are as follows. The SPV system has a 400 V output voltage rating with a 1 kW capacity. The load being considered is a three-phase, 1 hp squirrel cage IM connected at 415 V and 50 Hz.

The voltage control has been set up to satisfy each of the following requirements:

(1) Decentralized control is achieved normally;
(2) Under diverse system situations, the whole MG closed-loop model is stable;
(3) All of the associated DGs follow the reference signal that the SVM algorithm provides.

Each controller must successfully uphold the three requirements mentioned earlier and offer reliable control inside its application domain. The software platform MATLAB/Simulink has been used to implement the entire system. The SVM method is used to evaluate whether a PV system connected to a grid can improve power quality at the consumer terminals. Figure 7 depicts the creation of the SVM signal. The voltage waveforms and the current waveform share some phase and are both sinusoidal, as shown in Figure 8. Figure 9 illustrates how the speed of 1425 rpm was achieved while the load torque remained constant at 3.0 N-m, as shown in Figure 10. In accordance with carrier frequencies of 1 kHz and an MI of 0.9 (Figure 11), Figure 12 displays an FFT analysis of the current and voltage in the system under consideration. The THD_i and THD_v values were, respectively, 1.10% and 1.22%. Figure 13 depicts the voltage in the dc-link capacitor.

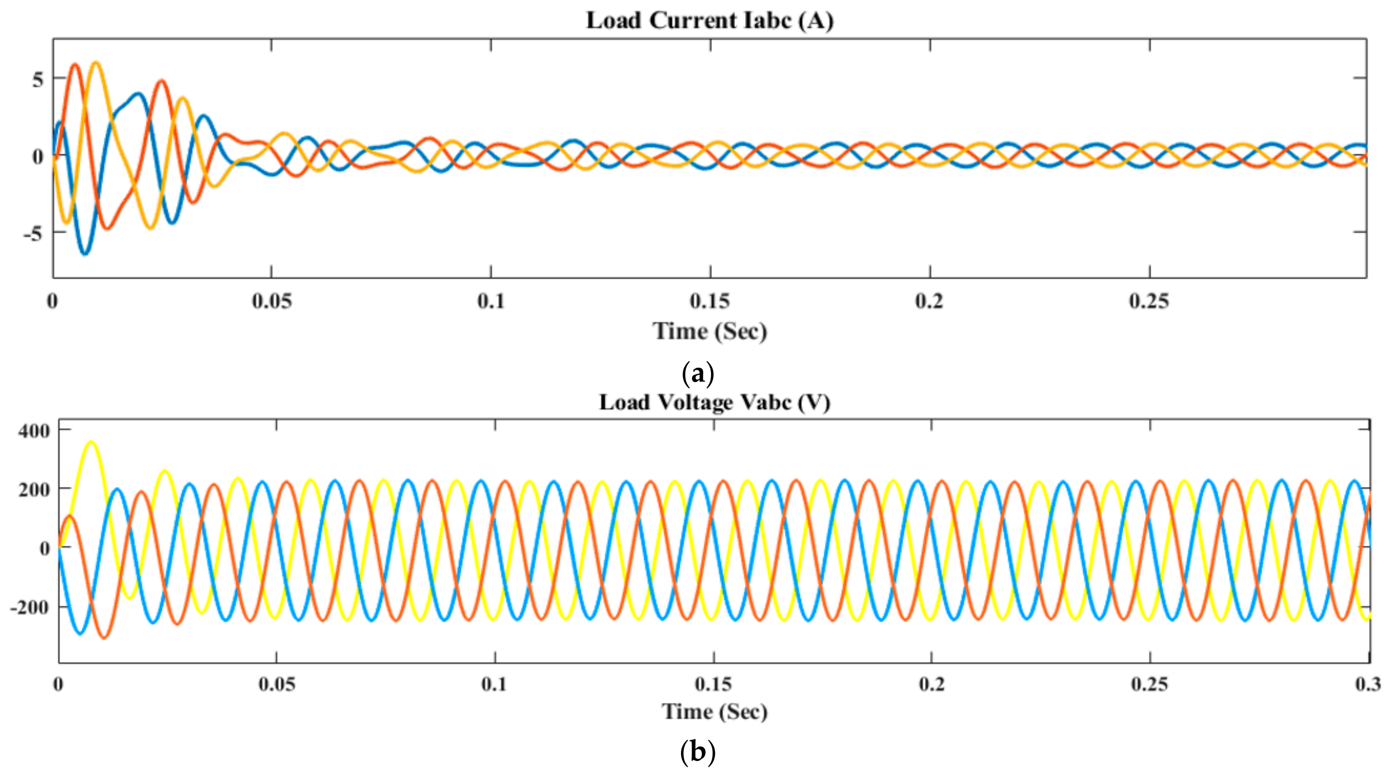

Figure 8. (**a**) Current and (**b**) Voltage waveform of the IM with the VOC-based SVM Controller.

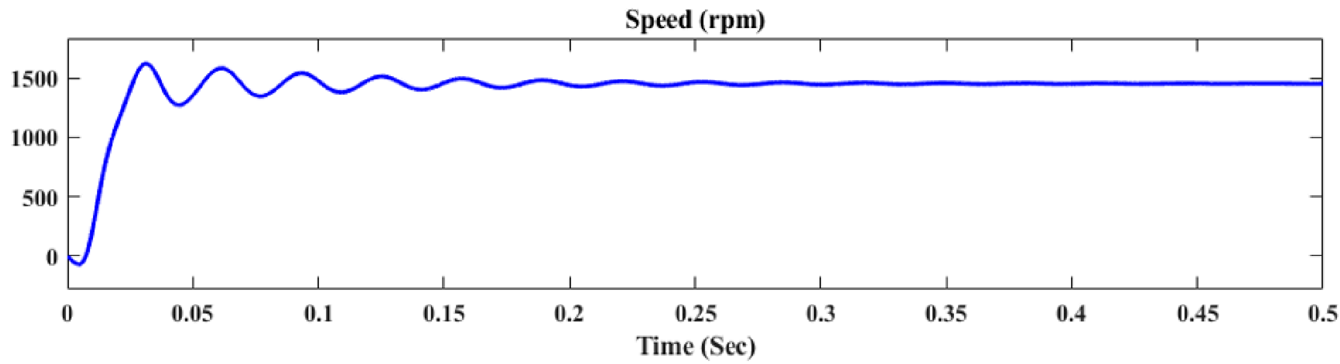

Figure 9. Speed of the Induction Motor when MI = 0.9.

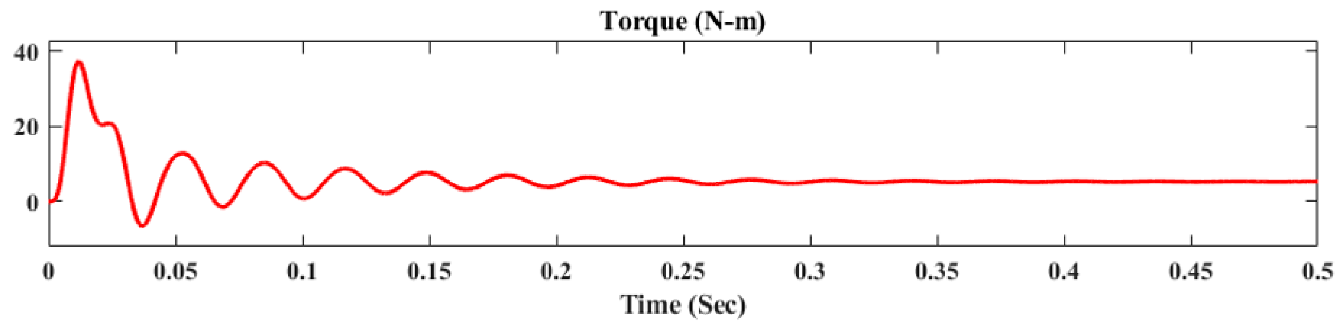

Figure 10. Torque of the Induction Motor.

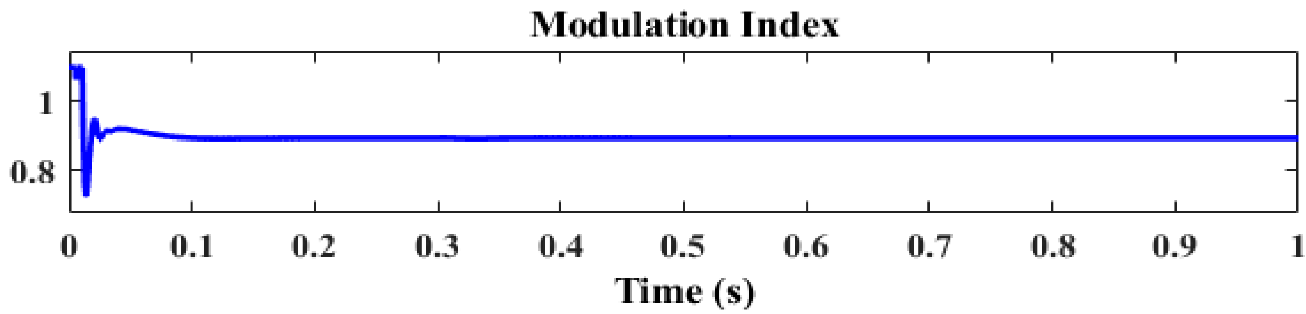

Figure 11. Modulation Index.

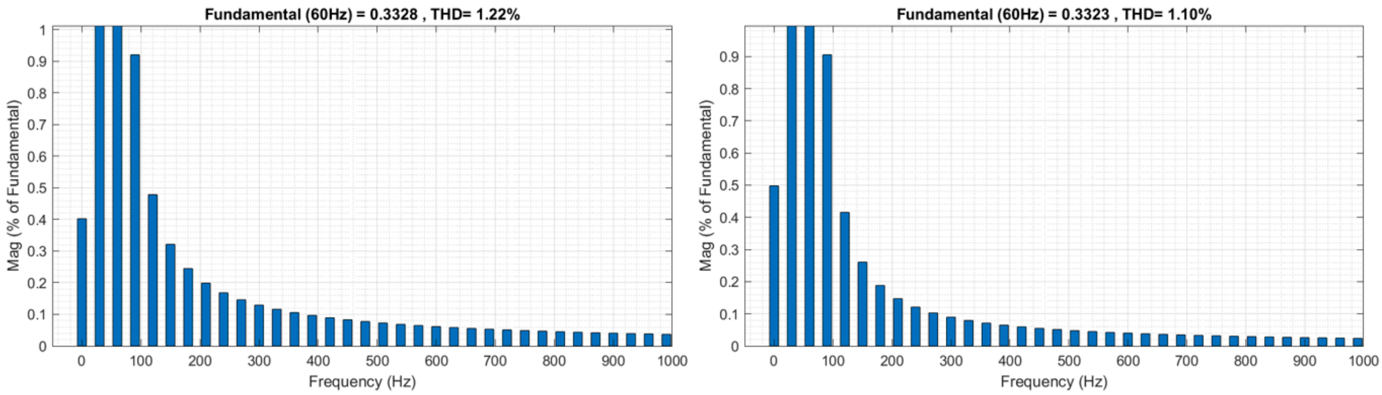

Figure 12. FFT analysis of the voltage and current of the Induction Motor.

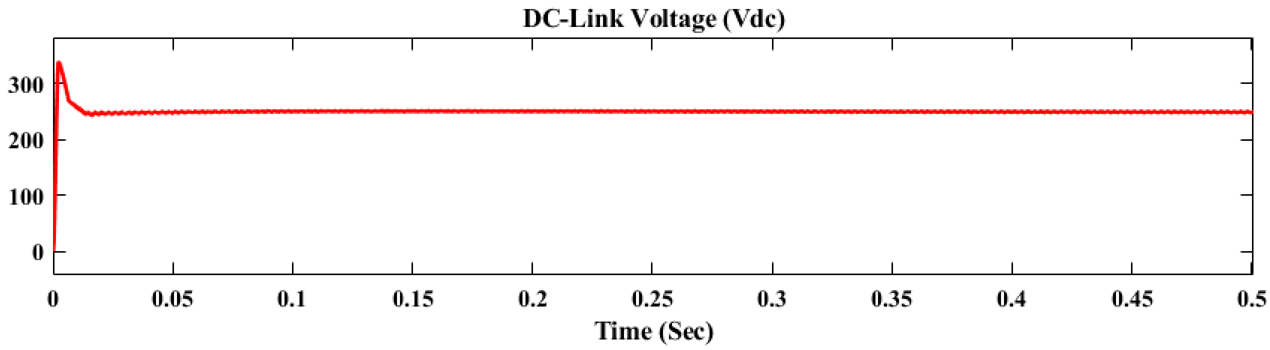

Figure 13. DC-Link voltage.

5.2. Experimental Verification of the Control Scheme

The efficiency of the suggested VOC-SVM control-based PI controller, shown in Figure 3, has been tested using a suitable configuration. Its primary components are a Fluke power quality analyzer, three-phase inverter, dSPACE kit, power analyzer, and PV simulator. A PVS1010 PV emulator with dc programming is used to determine the panel properties. A real-time dSPACE DS1104 controller interface controls the system by conditioning each field signal. A dSPACE platform, shown in Figure 14, is used to integrate the Simulink model with the external hardware. A D/A converter is used to interface the inverter gating signals with dSPACE. A dSPACE DS1104 board is used to run Simulink, which has been used to implement the simulated design modelling. The suggested control's main benefit is the ability to precisely adjust the THD and dc-link voltage. The testing was carried out using the MATLAB/Simulink interfaced dSPACE platform to realize the adequate performance of a VOC-SVM control-based grid-connected PV system.

For this reason, it was assumed that the grid phase voltage was 415 V with a frequency of 50 Hz and dc-link voltages of 250 V. The practical response to a dc-link voltage and SVM switching pulse is illustrated in Figure 15. The test results clearly show that the SVM-based VOC controller optimizes the dc-link voltage.

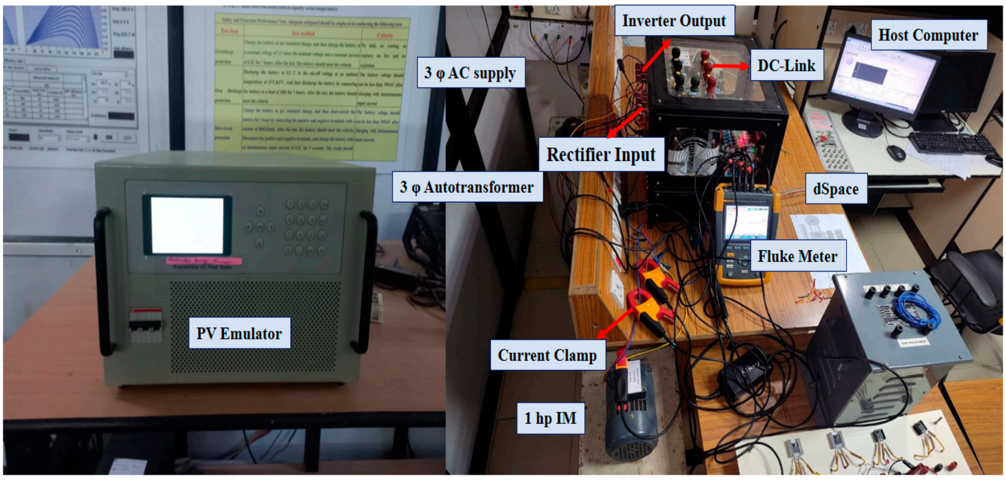

Figure 14. Experimental Setup of the three-phase inverter with VOC control using dSpace.

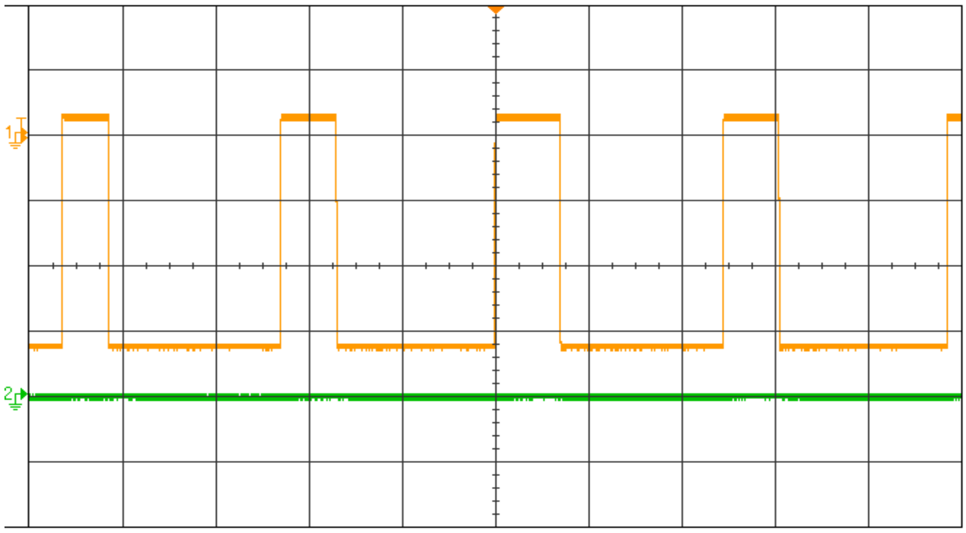

Figure 15. SVM Switching Pulse and DC-Link Voltage.

According to the IEEE 519 standard and Figure 14, an SVM based on ripple control was used to achieve reduced THD and described with the FFT spectrum of grid current under steady-state and dynamic operating circumstances. The waveforms were observed using a Fluke-43 spectrum analyzer with online numerical value illustration. The experimental voltage and current waveform of an inverter with a THD_i and THD_v for a modulation index of 0.3 are shown in Figure 16a–d.

Figure 17 depicts the voltage and current waveform with an FFT analysis with an MI of 0.6. Similarly, Figures 18 and 19 illustrate the voltage and current waveforms with FFT analysis for an MI of 0.9 using SPWM and SVM inverters.

Figures 16–19 illustrate output current waveforms with various modulation indices for comparison. It can be seen that when the MI is fixed at 0.9, the output current waveform is more sinusoidal. THD_i and THD_v results for various modulation indices are similarly displayed. The optimum output signal is created by increasing the MI with the SVM technique, as can be seen in Figure 20. It is also evident that increasing the MI results in a decrease in current and voltage harmonics. Figure 21 shows the change in speed with MI. The comparative analysis of the hybrid system with THDs with different modulation indices is shown in Table 1.

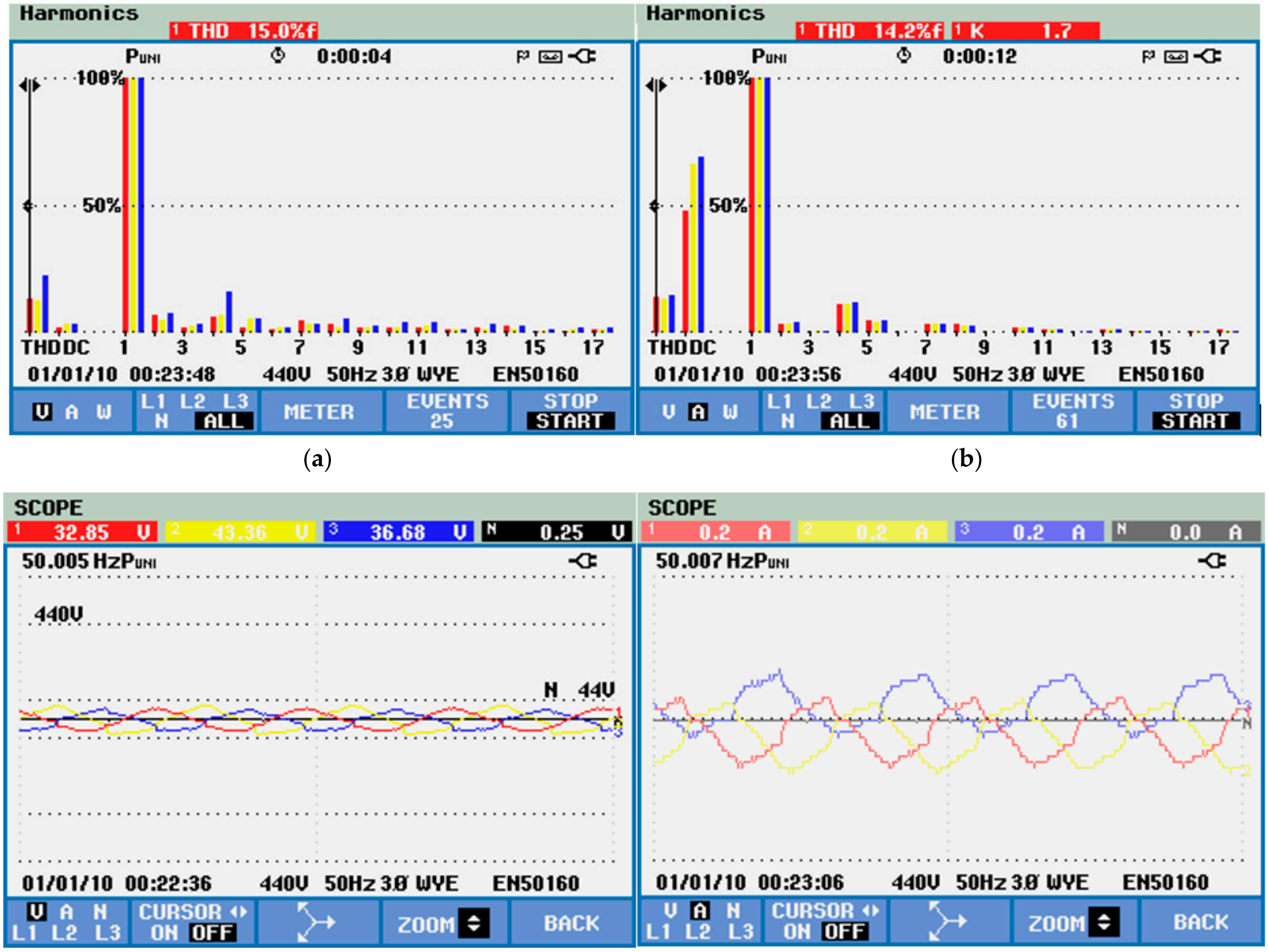

(**a**) (**b**)

(**c**) (**d**)

Figure 16. (**a**) Voltage THD (**b**) Current THD (**c**) Voltage (**d**) Current of a three-phase SVM inverter (**MI** = 0.3).

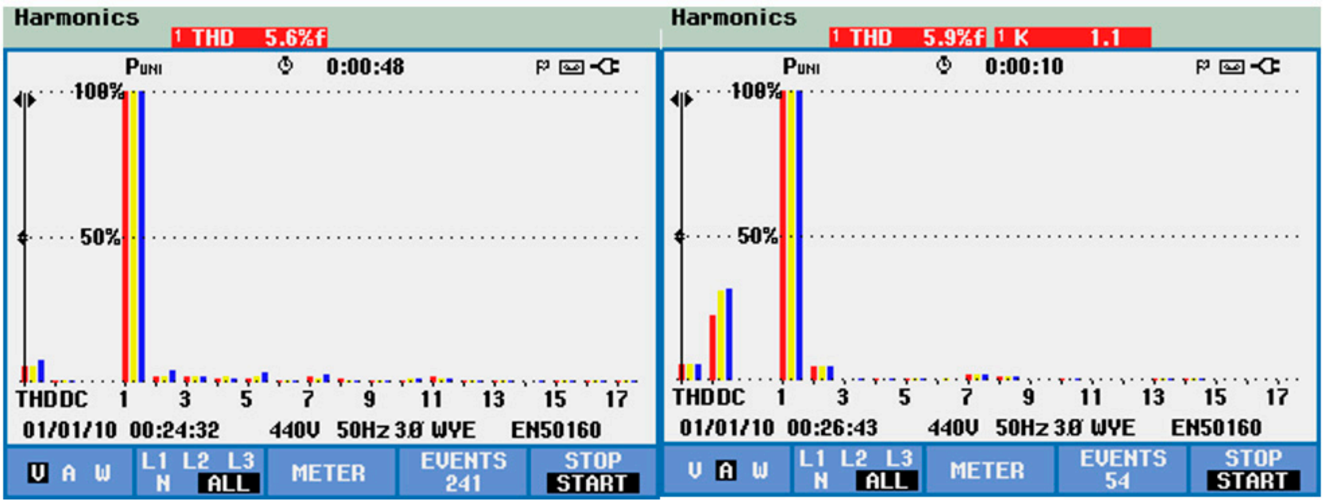

(**a**) (**b**)

Figure 17. *Cont.*

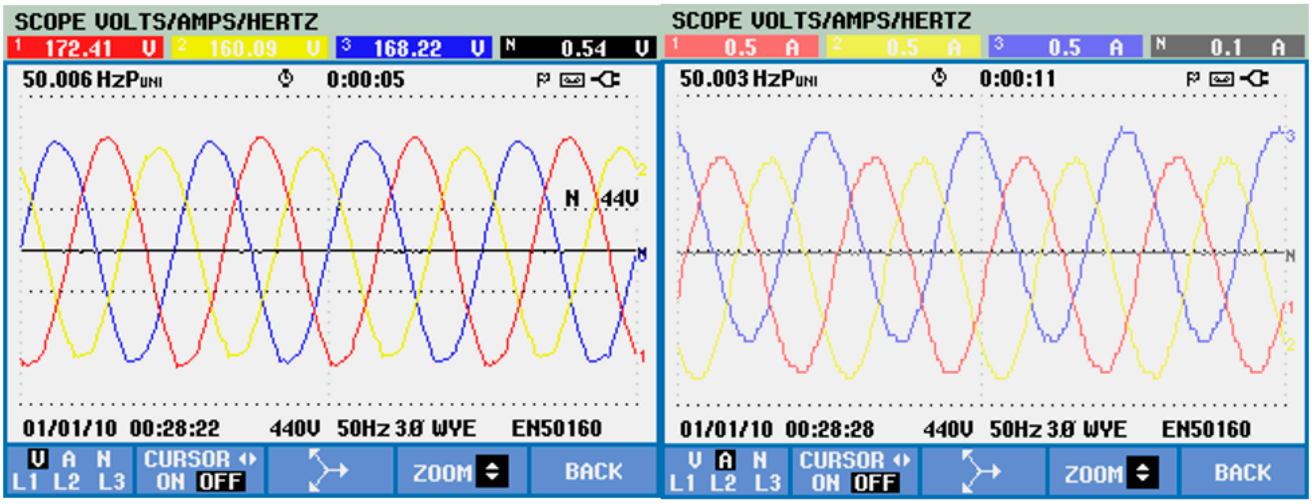

(**c**) (**d**)

Figure 17. (**a**) Voltage THD (**b**) Current THD (**c**) Voltage (**d**) Current of a three-phase SVM inverter (**MI = 0.6**).

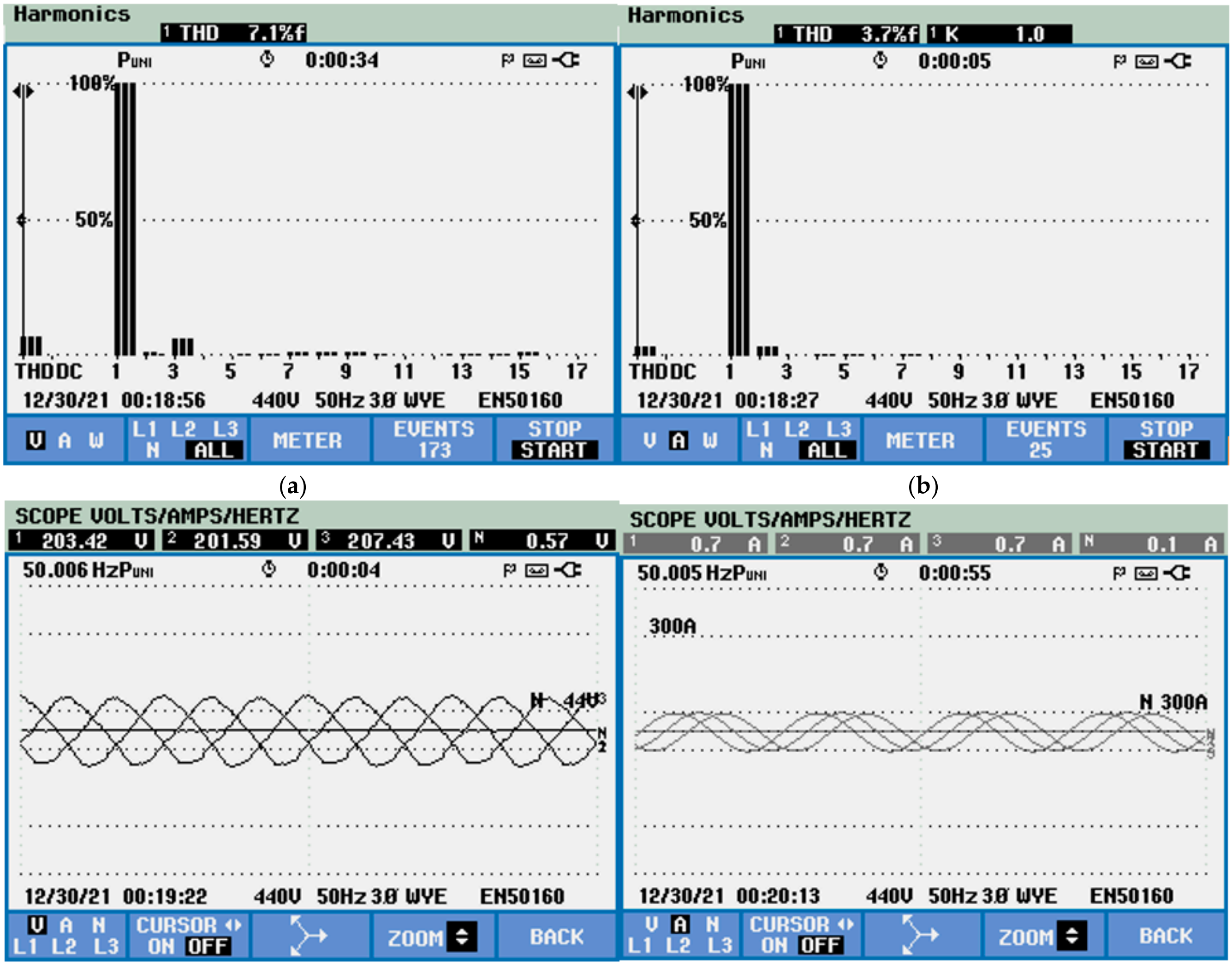

(**a**) (**b**)

(**c**) (**d**)

Figure 18. (**a**) Voltage THD (**b**) Current THD (**c**) Voltage (**d**) Current of a three-phase SPWM inverter (**MI = 0.9**).

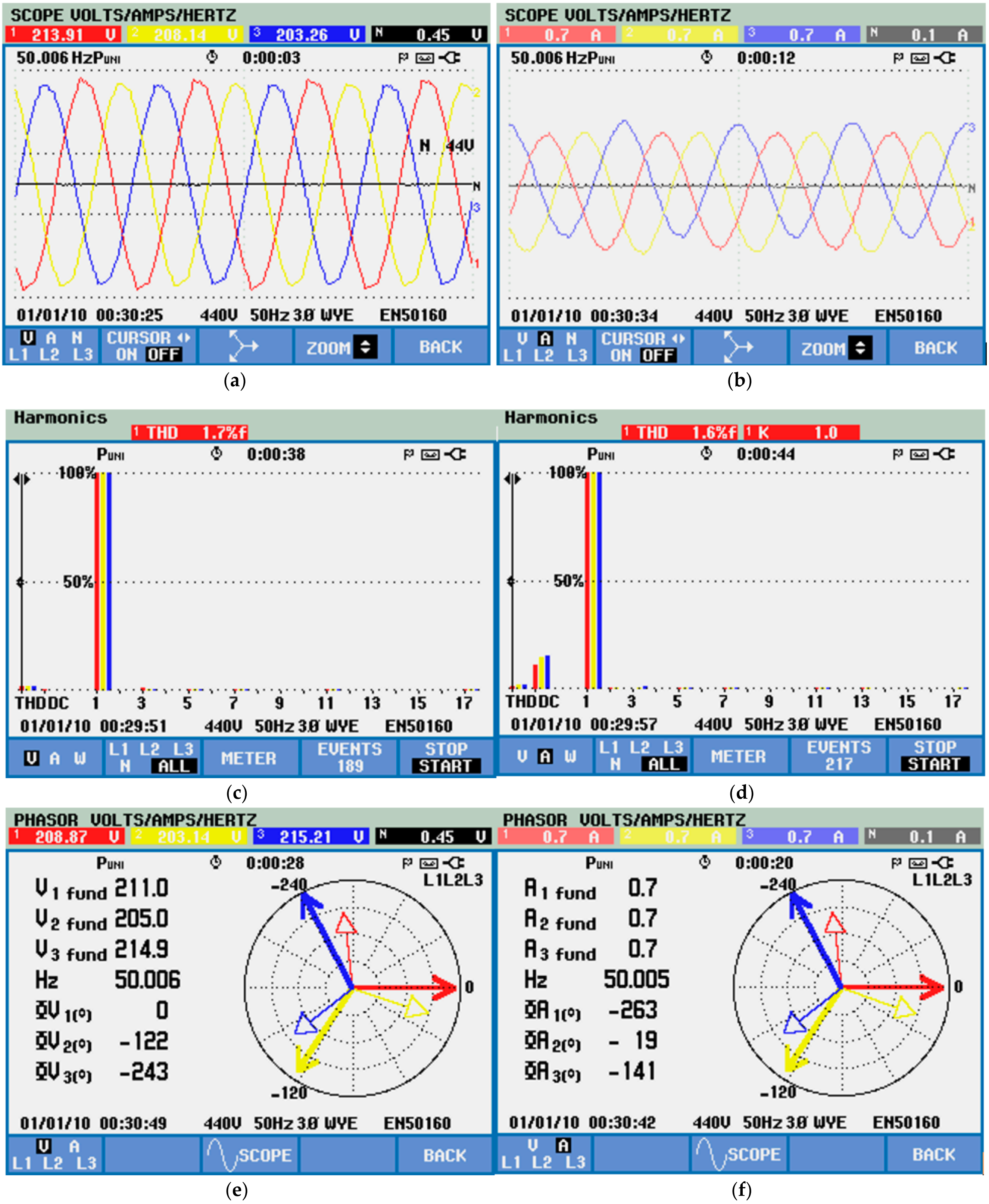

Figure 19. (**a**) Voltage (**b**) Current (**c**) Voltage THD (**d**) Current THD (**e**) Voltage and (**f**) Current Phasor Diagrams of a three-phase SVM inverter (**MI = 0.9**).

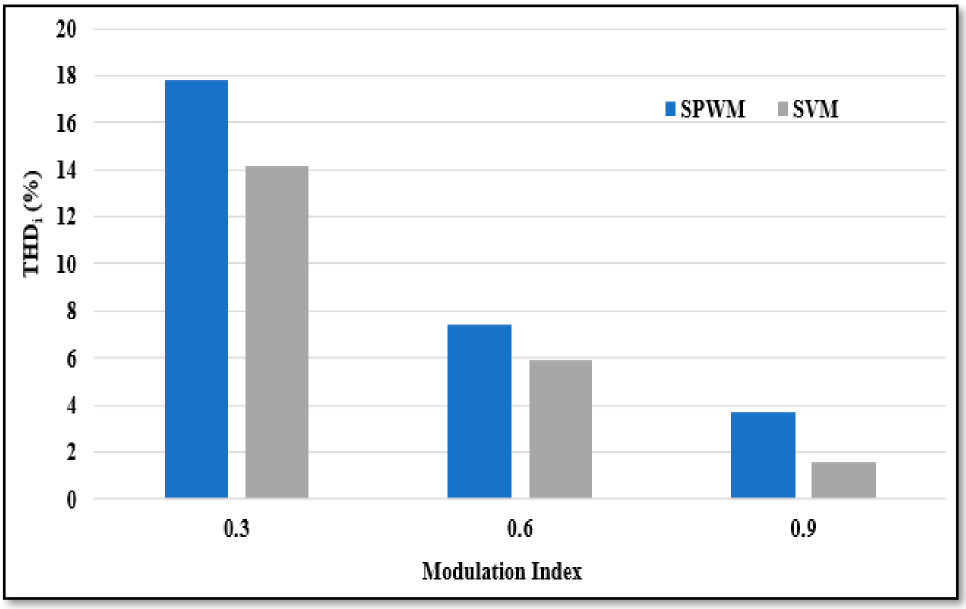

Figure 20. Comparison of Current THDs for the SPWM and SVM techniques.

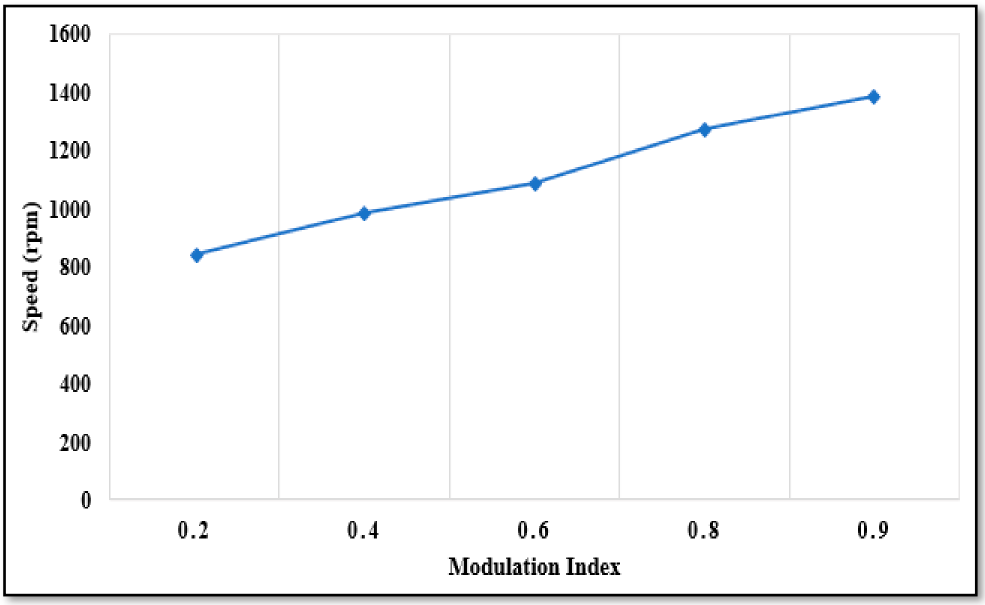

Figure 21. Change in speed vs. MI.

Table 1. Comparative analysis of THD with different modulation indices.

M.I	SPWM		SVM		Speed (rpm)
	THD$_i$ (%)	THD$_v$ (%)	THD$_i$ (%)	THD$_v$ (%)	
0.3	17.8	21.7	14.2	15.0	922
0.6	7.4	11.5	5.6	5.9	1138
0.9	3.7	7.1	1.6	1.7	1410

5.3. Power-Loss Analysis

Power loss is the most crucial factor when calculating an inverter's efficiency. The most power is lost at the power switches. Knowing the power loss and heat dissipation, in addition to the inverter efficiency, is critical for constructing the proper heat sink. Total power losses in semiconductor power switches are often classified as static or dynamic.

The static loss includes conversion loss (on-state power losses) and cut-off loss. Failure to switch on and turn off makes up for the dynamic loss. The switching loss (P_{sw}), conduction loss (P_{cond}), and blocking loss ($P_{blocking}$) are the three primary losses to calculate in power switches. The blocking losses caused by leakage currents must be noted, though they are usually overlooked. However, switching losses are insignificant. The huge reduction in switching losses in VSI devices is the consequence of the on-and-off switch procedure during one fundamental period [41]. The switching device used in the VSI is Si-MOSFET.

$$P_{Loss} = P_{Sw} + P_{Cond} + P_{blocking} \tag{40}$$

5.3.1. Conduction Losses

The conduction power losses (P_{cond}) of MOSFETs may be calculated using a MOSFET approximation of the drain-to-source resistance (R_{DSon}) [42].

$$V_{DS}(i_D) = R_{DSon}(i_D).i_D \tag{41}$$

where V_{DS}, i_D = root mean square of the drain-to-source voltage and the drain current. R_{DSon} can be determined by reference to the MOSFET datasheet because it depends on the gate-to-source voltage, the junction temperature (T_j), and the drain current (V_{GS}).

Equation (42) provides the instantaneous MOSFET conduction power.

$$P_{C,MOSFET}(t) = V_{DS}(t)i_D(t) = R_{DSon}i_D^2(t) \tag{42}$$

The following is an expression for the average conduction losses.

$$P_{C,MOSFET} = \frac{1}{T_{SW}}\int_{0+\varnothing}^{T_{on}} P_{C,MOSFET}(t)dt \tag{43}$$

T_{on} = on-state period and φ = the phase angle.

$$P_{C,MOSFET} = R_{DSon}i_{Drms}^2 \tag{44}$$

It is also possible to determine a body diode's ($P_{cond,diode}$) conduction loss using its resistance dynamics ($R_{on,diode}$) and diode threshold voltage (V_T), as demonstrated below:

$$P_{Cond,diode} = V_T I_{avg} + R_{on,diode} I_{rms}^2 \tag{45}$$

5.3.2. Switching Losses

Switching losses occur due to the slow transition from the on-state to the off-state and vice versa. Significant instantaneous power losses arise due to current flow and voltage via the switch becoming much more important than zero during the transition time [43].

During the turn-on interval, the energy dissipated.

$$E_{SW,MOSFET(on)} = \left(V_{dc}I_{dc}\frac{t_{c(on)}}{6}\right) - (V_{dc} - V_{on})I_{dc}\frac{t_{c(on)}}{3} \tag{46}$$

where $t_{c(on)}$ = the turn-on crossover interval and $E_{Sw}(on)$ = energy dissipated during the turn-on interval.

When the MOSFET was turned off, the energy dissipated.

$$E_{SW,MOSFET(off)} = \left(V_{dc}I_{dc}\frac{t_{c(off)}}{6}\right) - V_{on}I_{dc}\frac{t_{c(on)}}{3} \tag{47}$$

The total energy during turn-on and -off is:

$$E_{SW,MOSFET} = E_{SW,MOSFET(on)} + E_{SW,MOSFET(off)} \tag{48}$$

The switching losses had linear relations to the switching frequency and the switching current. The general average losses from swapping can be expressed as follows.

$$P_{SW,MOSFET} = \frac{1}{T_{SW}} \int_{0+\varnothing}^{T_{on}} E_{SW,MOSFET}dt \tag{49}$$

Figure 22 shows the power-loss analysis of the MOSFET-fed three-phase inverter.

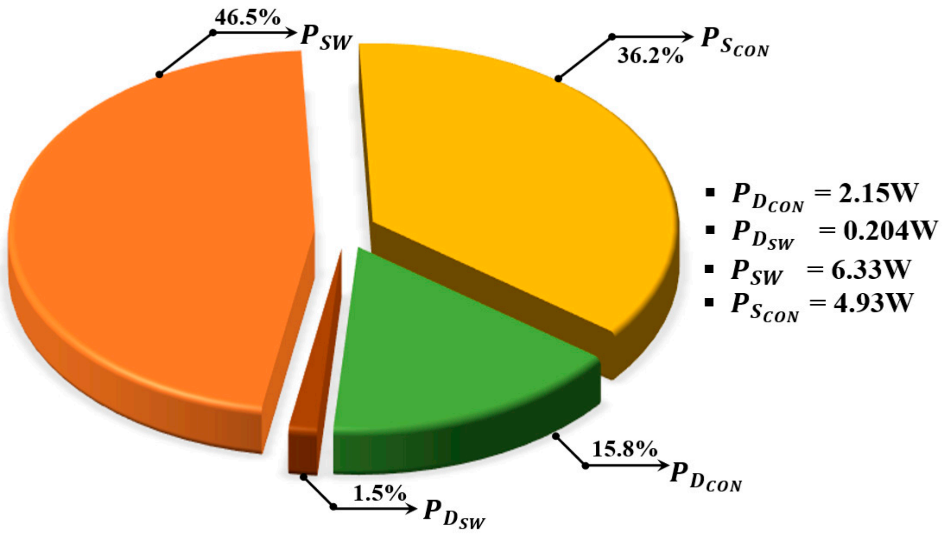

Figure 22. Power-Loss Analysis of Inverter.

6. Conclusions

In this study, SVM employing a PI controller was evaluated after considering the negative impacts of harmonics in a power system network. An SVM control technique was devised to reduce current harmonics and increase power quality. Pollution-free electricity generation via PV systems was prioritized along with improving power quality. This research paper focused on the harmonic analysis of a three-phase PWM inverter that supplies an IM using a variety of modulation indices. However, the work was limited, since losses were higher at high switching frequencies. The motor's speed can be controlled by creating suitable controls and switching methods. Since it can reduce switching losses and harmonic output signals, SVM is the ideal method for switching and regulating the inverter. In MATLAB, the three-phase PWM inverter that supplies the IM was modelled. An experimental setup was also created to validate the outcomes of the simulation. The results indicated that the IEEE Standard 519 limit of 5% for harmonic content in voltage and current was exceeded.

Additionally, it was found that THD declined as the MI rose. Future research could use various PWM techniques to reduce harmonics while maintaining constant MIs. Finally, the system was evaluated using a real-time scaled-down prototype based on dSPACE, and the simulation results were confirmed. Each scenario's harmonic analysis was adequately adjusted to the IEEE-519 Standard's limitations.

Author Contributions: Conceptualization. S.V., V.I., B.A. and M.B; Methodology. S.V., V.I. and M.B.; Software. S.V., Formal Analysis. S.V., V.I. and B.A.; Investigation. S.V.; Resources. S.V. and M.B.; Data Curation. S.V., V.I. and M.B.; Writing–original draft preparation. S.V. and V.I.; Writing—reviewing and editing. S.V., V.I. and B.A.; Visualization. V.I.; Supervision. B.A. and V.I. All authors provided critical feedback and collaborated in the paper. All authors have read and agreed to the published version of the manuscript.

Funding: This research received no external funding.

Institutional Review Board Statement: Not Applicable.

Informed Consent Statement: Not Applicable.

Data Availability Statement: Not Applicable.

Conflicts of Interest: The authors declare no conflict of Interest.

References

1. Lu, S.-M. A review of high-efficiency motors: Specification, policy, and technology. *Renew. Sustain. Energy Rev.* **2016**, *59*, 1–12. [CrossRef]
2. De Almeida, A.T.; Fong, J.; Falkner, H.; Bertoldi, P. Policy options to promote energy efficient electric motors and drives in the EU. *Renew. Sustain. Energy Rev.* **2017**, *74*, 1275–1286. [CrossRef]
3. Alsofyani, I.M.; Idris, N.R.N. A review on sensorless techniques for sustainable reliablity and efficient variable frequency drives of induction motors. *Renew. Sustain. Energy Rev.* **2013**, *24*, 111–121. [CrossRef]
4. Santos, T.H.d.; Goedtel, A.; da Silva, S.A.O.; Suetake, M. Scalar control of an induction motor using a neural sensorless technique. *Electr. Power Syst. Res.* **2014**, *108*, 322–330. [CrossRef]
5. Kashif, S.A.R.; Saqib, M.A.; Zia, S. Implementing the induction-motor drive with four-switch inverter: An application of neural networks. *Expert Syst. Appl.* **2011**, *38*, 11137–11148. [CrossRef]
6. Saidur, R.; Mekhilef, S.; Ali, M.B.; Safari, A.; Mohammed, H.A. Applications of variable speed drive (VSD) in electrical motors energy savings. *Renew. Sustain. Energy Rev.* **2012**, *16*, 543–550. [CrossRef]
7. Reza, C.M.F.S.; Islam, M.D.; Mekhilef, S. A review of reliable and energy efficient direct torque-controlled induction motor drives. *Renew. Sustain. Energy Rev.* **2014**, *37*, 919–932. [CrossRef]
8. Saidur, R. A review on electrical motors energy use and energy savings. *Renew. Sustain. Energy Rev.* **2010**, *14*, 877–898. [CrossRef]
9. Lipu, M.S.H.; Karim, T.F. Energy ef_ciency opportunities and savings potential for electric motor and its impact on GHG emissions reduction. *Int. J. Elect. Comput. Eng.* **2013**, *3*, 533–542.
10. Hannan, M.A.; Ali, J.A.; Mohamed, A.; Hussain, A. Optimization techniques to enhance the performance of induction motor drives: A review. *Renew. Sustain. Energy Rev.* **2017**, *81*, 1611–1626. [CrossRef]
11. Jannati, M. A review on variable speed control techniques for ef_cient control of single-phase induction motors: Evolution, classi_cation, comparison. *Renew. Sustain. Energy Rev.* **2017**, *75*, 1306–1319. [CrossRef]
12. Saad, N.; Arro, M. A PLC-based modi_ed-fuzzy controller for PWM-driven induction motor drive with constant V/Hz ratio control. *Robot. Comput.-Integr. Manuf.* **2012**, *28*, 95–112. [CrossRef]
13. Saribulut, L.; Teke, A.; Tümay, M. Vector-based reference location estimating for space vector modulation technique. *Electr. Power Syst. Res.* **2012**, *86*, 51–60. [CrossRef]
14. Vashishtha, S.; Rekha, K.R. A survey: Space vector PWM (SVPWM) in 3φ voltage source inverter (VSI). *Int. J. Electr. Comput. Eng. (IJECE)* **2018**, *8*, 11–18. [CrossRef]
15. Al-Ogaili, A.S.; Aris, I.B.; Verayiah, R.; Ramasamy, A.; Marsadek, M.; Rahmat, N.A.; Al-Masri, A.N. A three-level universal electric vehicle charger based on voltage-oriented control and pulse-width modulation. *Energies* **2019**, *12*, 2375. [CrossRef]
16. Young, H.A.; Perez, M.A.; Rodriguez, J.; Abu-Rub, H. Assessing finite-control-set model predictive control: A comparison with a linear current controller in two-level voltage source inverters. *IEEE Ind. Electron. Mag.* **2014**, *8*, 44–52. [CrossRef]
17. Liu, C.; Ma, R.; Bai, H.; Gechter, F.; Gao, F. A new approach for FPGA based real-time simulation of power electronic system with no simulation latency in subsystem partitioning. *Int. J. Electr. Power Energy Syst.* **2018**, *99*, 650–658. [CrossRef]
18. Gdaim, S.; Mtibaa, A.; Mimouni, M.F. Design and experimental implementation of DTC of an induction machine based on fuzzy logic control on FPGA. *IEEE Trans. Fuzzy Syst.* **2015**, *23*, 644–655. [CrossRef]
19. Hakami, S.S.; Mohd Alsofyani, I.; Lee, K.B. Low-speed performance improvement of direct torque control for induction motor drives fed by three-level NPC inverter. *Electronics* **2020**, *9*, 77. [CrossRef]
20. Wilamowski, B.M.; Irwin, J.D. *Power Electronics and Motor Drives*; CRC Press: Boca Raton, FL, USA, 2011.
21. Djoudi, A.; Bacha, S.; Iman-Eini, H.; Rekioua, T. Sliding mode control of DFIG powers in the case of unknown _ux and rotor currents with reduced switching frequency. *Int. J. Electr. Power Energy Syst.* **2018**, *96*, 347–356. [CrossRef]
22. Barnes, M. *Practical Variable Speed Drives and Power Electronics*; Newnes: Oxford, UK, 2003.
23. Singh, A.; Grant, B.; DeFour, R.; Sharma, C.; Bahadoorsingh, S. A review of induction motor fault modeling. *Electr. Power Syst. Res.* **2016**, *133*, 191–197. [CrossRef]
24. Chan, T.-F.; Shi, K. *Applied Intelligent Control of Induction Motor Drives*; Wiley: Hoboken, NJ, USA, 2011.
25. Krause, P.C.; Wasynczuk, O.; Sudhoff, S.D.; Pekarek, S. *Analysis of Electric Machinery and Drive Systems*; IEEE: Piscataway, NJ, USA, 2013.
26. Gandoman, F.H. Review of FACTS technologies and applications for power quality in smart grids with renewable energy systems. *Renew. Sustain. Energy Rev.* **2018**, *82*, 502–514. [CrossRef]
27. Abu-Rub, H.; Iqbal, A.; Guzinski, J. *High Performance Control of AC Drives with Matlab/Simulink Models*; Wiley: Hoboken, NJ, USA, 2012.
28. Talla, J.; Leu, V.Q.; Mídl, V.; Peroutka, Z. Adaptive speed control of induction motor drive with inaccurate model. *IEEE Trans. Ind. Electron.* **2018**, *65*, 8532–8542. [CrossRef]

29. Hannan, M.A. A quantum lightning search algorithm-based fuzzy speed controller for induction motor drive. *IEEE Access* **2018**, *6*, 1214–1223. [CrossRef]
30. Al-Ogaili, A.S.; Aris, I.; Othman, M.L.; Hoon, Y.; Isa, D.; Azis, N.; Abbas, H.F. A review of Different Control Methods in Power Electronics. *J. Eng. Appl. Sci.* **2018**, *13*, 2242–2253.
31. Liang, W.; Wang, J.; Luk, P.C.-K.; Fang, W.; Fei, W. Analytical modeling of current harmonic components in PMSM drive with voltage source inverter by SVPWM technique. *IEEE Trans. Energy Convers.* **2014**, *29*, 673–680. [CrossRef]
32. Zhang, X.; Zhang, W.; Chen, J.; Xu, D. Deadbeat control strategy of circulating currents in parallel connection system of three-phase PWM converter. *IEEE Trans. Energy Convers.* **2014**, *29*, 406–417.
33. Guzman, H.; Barrero, F.; Duran, M.J. IGBT-gating failure effect on a fault-tolerant predictive current-controlled five-phase induction motor drive. *IEEE Trans. Ind. Electron.* **2015**, *62*, 15–20. [CrossRef]
34. Velander, E.; Kruse, L.; Wiik, T.L.; Wiberg, A.; Colmenares, J.; Nee, H.-P. An IGBT turn-ON concept offering low losses under motor drive dv/dt constraints based on diode current adaption. *IEEE Trans. Power Electron.* **2018**, *33*, 1143–1153. [CrossRef]
35. Agarwal, P.; Langer, N.; Bhat, A.H. Neural-network-based space vector pulse-width modulation for capacitor voltage balancing of three-phase three-level improved power quality converter. *IET Power Electron.* **2014**, *7*, 973–983.
36. Amiri, M.; Milimonfared, J.; Khaburi, D.A. Predictive torque control implementation for induction motors based on discrete space vector modulation. *IEEE Trans. Ind. Electron.* **2018**, *65*, 6881–6889. [CrossRef]
37. Bose, B.K. Scalar decoupled control of induction motor. *IEEE Trans. Ind. Appl.* **1984**, *IA-20*, 216–225. [CrossRef]
38. Durgasukumar, G.; Pathak, M.K. Comparison of adaptive neuro-fuzzy-based space-vector modulation for two-level inverter. *Int. J. Electr. Power Energy Syst.* **2012**, *38*, 9–19. [CrossRef]
39. Boby, M.; Gopakumar, K.; Umanand, L.; Blaabjerg, F.; Bhattacharya, S. A low-order harmonic elimination scheme for induction motor drives using a multilevel octadecagonal space vector structure with a single DC source. *IEEE Trans. Power Electron.* **2018**, *33*, 2430–2437. [CrossRef]
40. Kirankumar, B.; Reddy, Y.V.S.; Vijayakumar, M. Multilevel inverter with space vector modulation: Intelligence direct torque control of induction motor. *IET Power Electron.* **2017**, *10*, 1129–1137. [CrossRef]
41. Sumithira, T.R.; Nirmal Kumar, A. Elimination of harmonics in multilevel inverters connected to solar photovoltaic systems using ANFIS: An experimental case study. *J. Appl. Res. Technol.* **2013**, *11*, 124–132. [CrossRef]
42. Ahmed, M.H.; Wang, M.; Hassan, M.A.S.; Ullah, I. Power loss model and efficiency analysis of three-phase inverter based on SiC MOSFETs for PV applications. *IEEE Access* **2019**, *7*, 75768–75781. [CrossRef]
43. Chaturvedi, P.K.; Jain, S.; Agrawal, P.; Nema, R.K.; Sao, K.K. Switching losses and harmonic investigations in multilevel inverters. *IETE J. Res.* **2014**, *54*, 297–307. [CrossRef]